LA-UR-16-26672
Approved for public release; distribution is unlimited.

Title: Dense Plasma Focus Modeling

Author(s): Li, Hui
Li, Shengtai
Jungman, Gerard
Hayes-Sterbenz, Anna Catherine

Intended for: Report

Issued: 2016-08-31

Dense Plasma Focus Modeling

Hui Li, Shengtai Li, Gerard Jungman and Anna Hayes
Theoretical Division, Los Alamos National Laboratory
Los Alamos, NM 87544

Executive Summary

The mechanisms for pinch formation in Dense Plasma Focus (DPF) devices, with the generation of high-energy ions beams and subsequent neutron production over a relatively short distance, are not fully understood. Here we report on high-fidelity 2D and 3D numerical magnetohydrodynamic (MHD) simulations using the LA-COMPASS code to study the pinch formation dynamics and its associated instabilities and neutron production. Our main findings are that:

- In general, multiple pinches will be formed and these lead to multiple neutron pulses.
- The pinch formation can be controlled by the use of a reentrant tube, the so-called INNY, which limits the volume in which pinches can form.
- There is an optimum position at which the INNY should be placed, namely, 6.5 cm above the top of the anode. At this distance, one main pulse will be formed, preceded by a small pulse, often referred to as a 'front porch'.
- If the INNY is positioned closer than about 5.5 cm form the anode, the front porch becomes the main pulse and the second neutron pulse will appear as a small 'back-porch'.
- The timing of the front porch is independent of the INNY position, but the timing between this first pulse and the second neutron pulse increases as the INNY-to-anode distance is increased.
- The magnitude of the porches can be controlled by the position of the INNY. However, there appears to be no position at which the INNY can be placed to get rid of the small porches altogether. Thus, analyses of activation of objects using a DPF neutron source need to account for these deviations from a single clean pulse.
- The size (diameter) of the INNY can also be optimized to maximize the neutron yield, but not the time-shape of the pulse. The optimum INNY size is the one which is maximum and which closes possible exit of energy and ions out from the region between the INNY and the anode.

- The energy distribution of the neutron pulse provides a stringent test of the fidelity of the MHD simulations, and for DD gas it is predicted to be centered close to 3 MeV, with a very approximate Gaussian shape corresponding to a width of $\sigma = 0.2$. This is in very good agreement with experiment.

- Any perturbation in the azimuthal symmetry of the veocity of the current sheath affects pinch formation. Velocity asymmetries of 5% lead to kink instabilities in the pinch, and a very non-cylindrically shaped pinch. Asymmetries also shift the pinch formation off axis. 3D simulations are crucial for accurate description of these phenomena and DPF performance predictions.

- Determining the cause of asymmetries requires further experiments. But unwanted fluorescence effects can be caused by impurities, ionizing gas in front of the sheath, and causing sheath azimuthal velocity asymmetries.

- Any mechanical force (such as sparks induced by impurities) that causes the anode and cathode to be no longer concentric also leads to sheath velocity front asymmetries, preventing strong pinch and neutron pulse formation.

1 Introduction

A DPF Z pinch is a device consisting of two coaxially located electrodes with a high-voltage source at one end. In the presence of a low-pressure gas, the high-voltage source induces a surface flash-over and the formation of a current-conducting plasma sheath across an insulator at the upstream end of the DPF. During the so-called "run-down" phase, the current sheath is accelerated down the length of the electrodes by magnetic pressure, ionizing and sweeping up neutral gas as it accelerates. When the plasma sheath involved in the run-in reaches the end of the inner electrode, a portion is pushed radially inward during the so-called "run-in" phase. When the leading edge of the current sheath reaches the central axis, under the strong azimuthal magnetic pinch force, the plasma creates a hot, dense region (called a "pinch") that emits high-energy electron and ion beams, x rays, and (in the presence of D or D-T gas) neutrons.

Recent experiments have shown that the neutron time histories often show multiple pulses on the 50-300 nanosecond timescale. In addition, it is found that the use of a conducting plate (known as the "INNY"), placed several centimeters above the anode surface, can reduce the number of pulses, as well as the pulse duration. Key questions addressed in this work include the following. What are the mechanisms of pinch formation and what processes control the neutron pulse duration? What role does the INNY play? What design improvements are possible and what imperfections are likely to result in device failure?

2 Modeling

The DPF device is modeled as a cylindrical object depicted in Fig. 1. The radius of the anode is 7.6 cm, and the radial distance between the anode's outer wall and cathode's inner

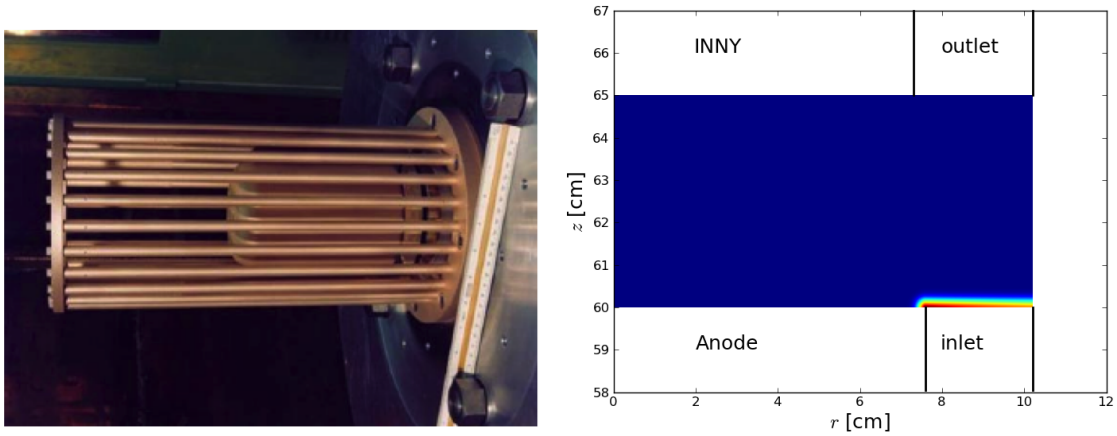

Figure 1: The cathode (24 copper bars) and anode (inside the cathode) of the DPF (left). The simulation setup (right) shows the arrangement in which both the anode ($0 < r < 7.6$ cm) and cathode ($10.2 < r < 12$ cm) are cylinders and the INNY (not shown on the left) is a plate placed parallel to the top surface of the anode. The blue-colored region in the simulation setup is filled with gas initially. The pinch forms near the $r = 0$ axis. Magnetic fields are initially injected between the anode and cathode walls, in the region labeled as the inlet. We note that the figure on the left is rotated 90 degrees with respect to the figure on the right.

wall is 2.6 cm. The length of the anode is 60 cm, The radius of the INNY can vary between 0 (no INNY) to 10.2 cm (in which case the INNY fully closes up the outlet).

As we are primarily focused on the dynamics of pinch formation and its consequences, our simulations will mostly concentrate on the "run-in" phase. This phase begins when the plasma sheath reaches the top of the anode, after the run-down phase. During the run-down phase, the plasma sheath runs from the bottom to the top of the cylindrical anode. In the present analysis, we mimic the entire run-down phase with an injection process, which lasts for a finite time and which can either involve an axisymmetric 2-D injection, or a non-axisymmetric 3-D injection. The plasma drive through the run-down phase is often described in terms of a circuit model, which here we simplify into an injection of an azimuthal magnetic field B_ϕ over a finite time t_{inj} , as shown in the right panel of Fig. 1.

Part of our motivation for replacing the run-down phase with an injection process is that experimental images show that at the end of the run-down phase and the start of the run-in phase the current sheath is often azimuthally asymmetric. Modeling these asymmetries during the run-down phase would be extremely computationally expensive and challenging. Such studies are the focus of research by other teams [1]. In the present work, we have chosen to use as much experimental information as possible in order to describe the initial conditions of the run-in phase, which we do by varying the parameters describing the 2-D or 3-D injection process to match experimental sheath velocity profiles and asymmetries at these early times.

All of our simulations use normalized code units with the following conversion.

	density	velocity	time	length	B field	pressure
physical unit	#/cc	cm/s	μs	cm	Gauss	ergs/cc
1 code unit=	10^{14}	10^7	1	10	650	4×10^4

The simulation domain is taken as a cylinder $r \times z = [0, 1.02] \times [6, H_{\rm Inny}]$, where $H_{\rm Inny}$ is the height of the INNY from the anode. The radius of the INNY, $R_{\rm Inny}$, is a user-input parameter. We inject the magnetic fields from the $z = 6$ boundary with an inlet at $r \in [0.76, 1.02]$ (see Fig. 1). The profile for the injected magnetic fields is

$$B_\phi^{inj}(t) = \gamma_{b_\phi} t B_0 \left(\frac{0.76}{r}\right) \quad , \tag{1}$$

where γ_{b_ϕ} is the injection rate and B_0 is the value of B_ϕ at $r = 0.76$. The injection is implemented as

$$B_\phi^{t_{n+1}} = B_\phi^{t_n} + \gamma_{b_\phi} \Delta t B_0 \left(\frac{0.76}{r}\right) \quad . \tag{2}$$

The injection process lasts $t = t_{inj}$, which is also a user-input parameter. Typically, we have $t_{inj} = 0.44$, $\gamma_{b_\phi} = 10$, $B_0 = 555$. At the start of the process, the simulation region is filled with plasmas that have pressure $P_0 = 1.1976$ and density $\rho_0 = 10^4$.

The injected magnetic fields and their associated current produce a Lorentz force that pushes the plasma fluid upwards initially, mimicking the "run-down" stage. When the plasma reaches $z = 6$, the Lorentz force also pushes the plasma towards the $r = 0$ axis, which is the "run-in" stage. The anode, cathode, and INNY are treated as perfect conducting boundaries.

3 Numerical Method

We use a numerical package primarily developed at LANL, called Los Alamos COMPutational Atro-physical Simulation Suite (LA-COMPASS) ([2, 3, 4]). This suite is a collection of several modern, high resolution, Godunov-type, hydrodynamics and magnetohy-drodynamics (MHD) codes that have been developed at LANL over the past decade. In particular, we have used this package to study the dynamics of 3D astrophysical jets including their 2D sausage and 3D kink instabilities ([5, 6, 7]). The MHD solver in the LA-COMPASS package implements ideal MHD with adaptive mesh refinement (AMR), and has been extended to include solvers for heat conduction, resistivity, and viscosity. It is a Godunov-type method that requires a Riemann solver at cell interfaces. Currently, we have implemented HLLE, HLLC, HLLD, and Roe's approximate Riemann solvers for MHD. To obtain the Riemann states at cell interfaces with high-order accuracy, we have implemented the MUSCL Hancock linear method, Colella's multi-dimensional scheme for second-order method, PPM for third-order, and WENO for fifth-order methods for the reconstruction of the cell-interface values. We have also enhanced the AMR capabilities by preserving the conservative quantities and preserving the divergence free constraint for the magnetic field. The package is fully parallelized and optimized via hybrid MPI+OPENMP for large-scale parallel computers with multi-cores. LA-COMPASS includes solvers for Cartesian, cylindrical and spherical grid. We use the 2D (r, z) and 3D (r, ϕ, z) cylindrical grid to study the DPF problem.

We have tested different reconstruction methods and different Riemann solvers. The numerical methods fall into three categories:

1. dimensional split vs. dimensional unsplit; dimensional unsplit solver is usually better for MHD problem, but is more expensive.

2. methods of obtaining the Riemann states at cell interfaces: second-order linear reconstruction vs. higher-order reconstruction via piece-wise parabolic method (PPM).

3. Riemann solver: HLL vs. HLLD; HLLD is more accurate but more expensive.

Of the eight possible combinations of numerical methods, we compare four, namely:

1. method 1: dimensional split method with linear reconstruction and HLL Riemann solver,

2. method 2: dimensional split method with PPM reconstruction and HLL Riemann solver,

3. method 3: dimensional split method with PPM reconstruction and HLLD Riemann solver,

4. method 4: dimensional unsplit method with PPM reconstruction and HLLD Riemann solver.

We found that method 4 offered the highest accuracy for treating instabilities. These instabilities turn out to be crucial to any description of DPF pinch formation, and so we discuss the predictions from method 4 in detail below.

4 2D MHD Results

4.1 Kelvin-Helmholtz (K-H) Instability

We begin with a two-dimensional description of the pinch formation. During the run-in phase, the cylindrical current sheath (essentially un-magnetized) is being pushed by the Lorentz force towards the central axis at $r = 0$, while also expanding upwards. The sheath has a parabolic shape in the $\{r, z\}$ plane, as shown in Fig. 2. Exterior to this sheath is a magnetically dominated region, with low density. The interface between the current sheath and the magnetized region is also accelerating. This leads to an effective acceleration, which when coupled with the density and velocity differences across this interface, results in a K-H instability being excited (most likely by satisfying the Richardson number criterion). The K-H instability can be seen in the detailed density and magnetic field structures, Fig. 2.

The K-H instability causes density and velocity variations along the sheath front, which translate into a density variation along the $z-$direction, when the pinch finally forms near $r = 0$ axis. For this reason, the location and intensity of the first pinch is determined by the development of the K-H instability, as seen in Fig. 3. Thus a fully physical description of pinch formation requires a high-resolution description of K-H instabilities.

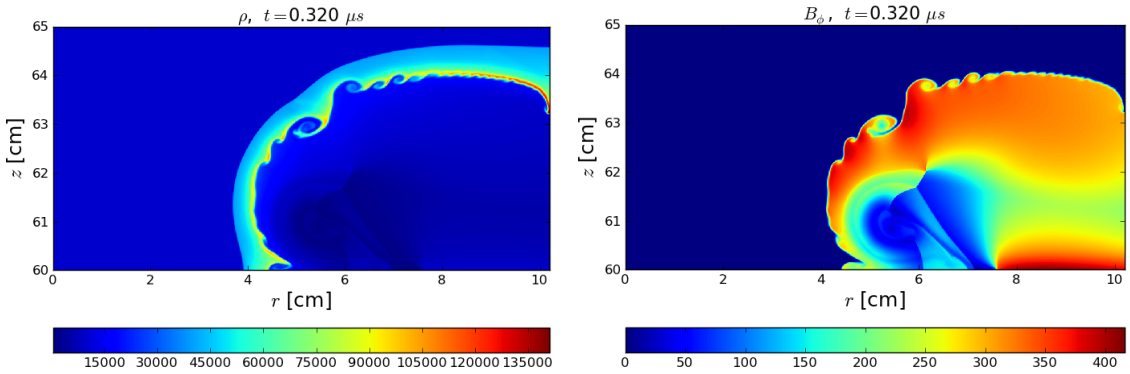

Figure 2: The K-H instability is seen in the density (ρ) and the magnetic field component (B_ϕ) distributions at 0.32 μs after the magnetic field injection. The density and magnetic field quantities are in code units.

5 The Neutron Production Mechanism

To calculate the neutron time histories, we developed a post-processor that accelerates and transports the D or T ions and produces neutrons through ion-ion beam-target interactions. In this section we describe the detailed physics involved in the neutron production, and our simulation tool.

Ions are accelerated from the thermal bath and into non-equilibrium streaming states by a kinetic mechanism which can be thought of as an "inverse straggling" process. At energies near the thermal energy, random up-scattering events allow some small fraction of ions to be accelerated by local EMFs, moving them away from the thermal peak. When their energy becomes large enough, the streaming process becomes entirely collisionless and the particles form a beam, moving in the direction of the large-scale EMF, which points in the vertical direction for the typical pinch geometry.

The energy of particles in the accelerated ion beam is determined simply by the voltage differences along the beam line, which in turn are determined by the MHD details. Given the energy distribution of the beam, it is straightforward to compute the beam-target interaction rate, which determines the neutron production rate. One significant difference between DD and DT pinch neutron production comes from the qualitative differences in the DD and DT reactions. The DD cross-section is essentially featureless in the regime of interest, rising steadily above the Coulomb barrier. On the other hand, the DT cross-section displays a strong resonance near 100 keV, so that beam ions in a DT plasma may be given an enhanced neutron production in the energy window around the resonance.

A basic assumption in the use of our post-processing framework is that the back-reaction on the ionized gas due to beam-generated fields is negligible compared to the forces due to global MHD fields. In other words, we assume that the beam current is small compared to the total system current, so that it does not affect the MHD. Simple estimates show that this condition is valid for all regimes examined in our simulations to date. We compute local EMF directly from the MHD predicted time and spatially dependent velocities, densities, temperatures, and electric and magnetic fields

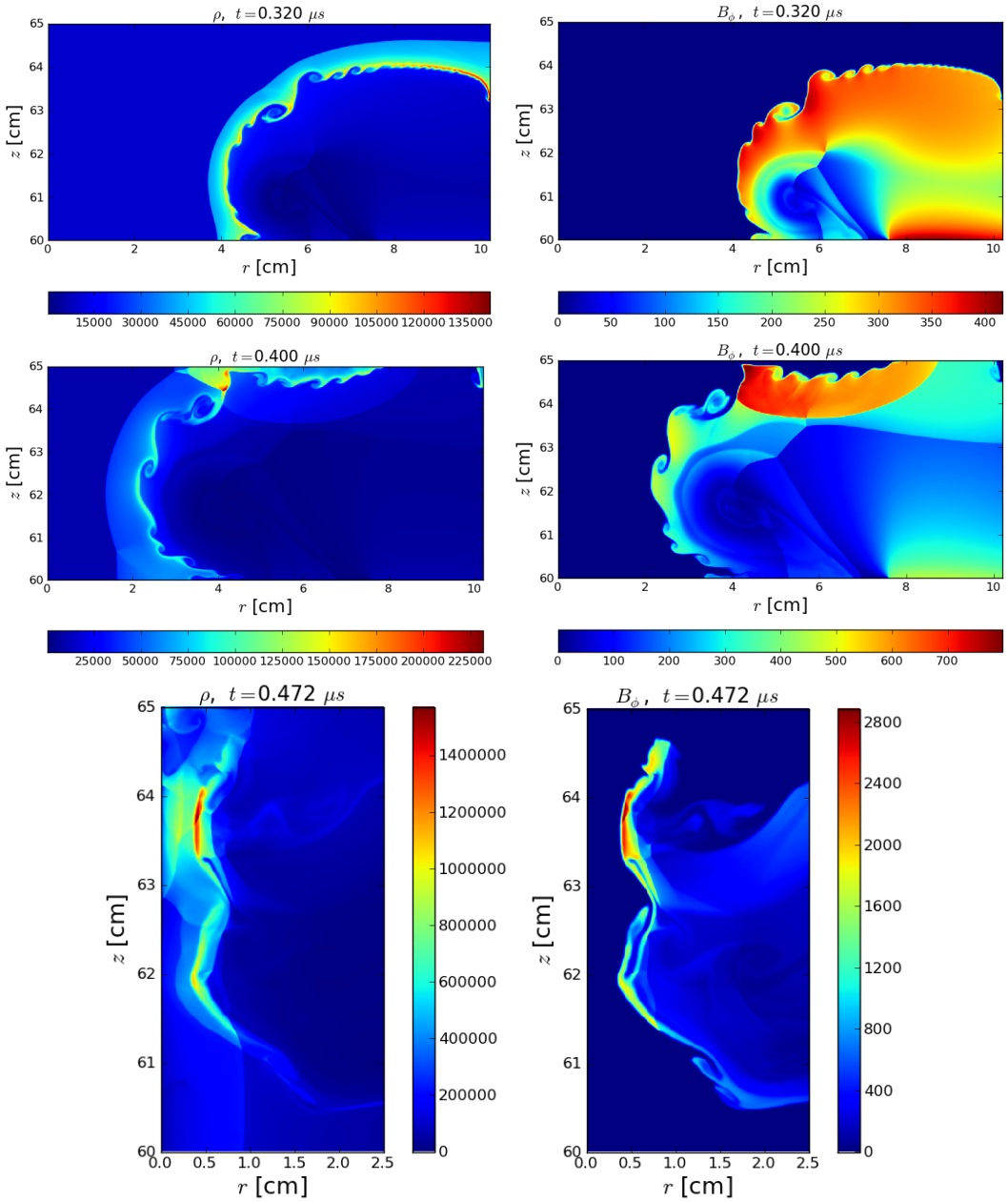

Figure 3: The evolution of density (left) and magnetic field (right) distributions approaching the pinch formation. In this simulation the INNY is located 5 cm from the anode surface, which is a standard location for the experiments. The reflection of the two distributions from the INNY surface is visible in the middle panels, though its impact on the initial pinch formation is likely small because the reflected component is lagging the main front. The initial location of the pinch is strongly influenced by the evolution of the K-H instabilities during the current sheath front propagation. The density and magnetic field quantities are in code units.

The computed local EMF is assumed to accelerate ions from the thermal bath into non-equilibrium streaming states, and uses a basic kinetic model for the selection of ionized particles from the bath. In this kinetic model, the local production rate of accelerated particles is proportional to the ion density and field strengths, with a kinetic coefficient which is undetermined at the level of the MHD simulation and which therefore introduces an overall normalization factor, which can be fixed by fixing a value for the beam current. The basic production mechanism, the relative energy distribution of the beam, and the relative energy distribution of produced neutrons are unaffected by this overall normalization. Also, the overall normalization has no effect on comparative design studies. Thus, though the overall predicted neutron yield is not normalized, the relative yields, the energy distributions, and the time histories are, and so the calculations provide detailed information on the effects of changes to the design of the anode, cathode and INNY on the neutron production. As discussed below, the excellent comparison between the measured and predicted neutron energy distributions strongly supports these arguments.

The distribution of the beam ions, differential in energy, and as a function of space and time, can be tracked straight-forwardly, because the acceleration depends entirely on the locally produced EMF, which is computed from the MHD data. In general, the neutron flux $d\phi_n(r,t)/dE_n$ in the forward direction at any point in time or space is given in terms of the accelerated ion beam by,

$$\frac{d\phi_n}{dE_n}(r,t) = \frac{1}{2\pi}\int dz \int_0^{V_{max}(t)} dE_b \frac{d\phi_B(r,z,t)}{dE_B} n_2(r,z,t)\sigma(E_B)\delta(E_n - \varepsilon(E_b)) \ . \tag{3}$$

Here $d\phi_B(r,z,t)/dE_B$ is the ion flux at (r,z,t), $V_{max}(t)$ is the maximum voltage difference seen by an ion at time t, $n_2(r,z,t)$ is the density of target ions seen by the beam at (r,z,t), $\sigma(E_B)$ is the DD or DT fusion cross section, and $\varepsilon(E_b)$ is the two-body kinematical factor needed to produce a neutron of energy E_n in the forward direction from a DD or DT reaction with an ion beam of energy E_B. The acceleration of ion beam also gets slowed by the plasma stopping power, and $d\phi_B(r,z,t)/dE_B \propto 1/dE/dX$ (Jungman and Hayes 2013 [8]). At long distances, the effect of stopping power must be taken into account. We estimate that the stopping length is several times the vertical extent of a typical pinch, so that stopping power is negligible for interactions within and near the pinch, where acceleration occurs. However, the neglect of stopping power will cause an overestimate of neutron production due to long-distance beam transport. It will also produce a neutron energy spectrum with an average energy that is too high. The detailed effects of stopping are currently under study.

5.1 The Neutron Energy Distribution

The energy distribution of the neutrons is determined by the energy of the ions inducing the DD or DT reactions, which is itself determined by the acceleration across the voltage differences seen by the ion, eq. (3). These voltage differences are determined by a number of MHD details, including the shape, velocity, and magnetic field of the current sheath. To a large extent, the final properties of the sheath at the time of neutron production are dominated by initial injection conditions at the inlet and the MHD propagation. In addition, the neutron production sees some affects from the the K-H instabilities. These instabilities

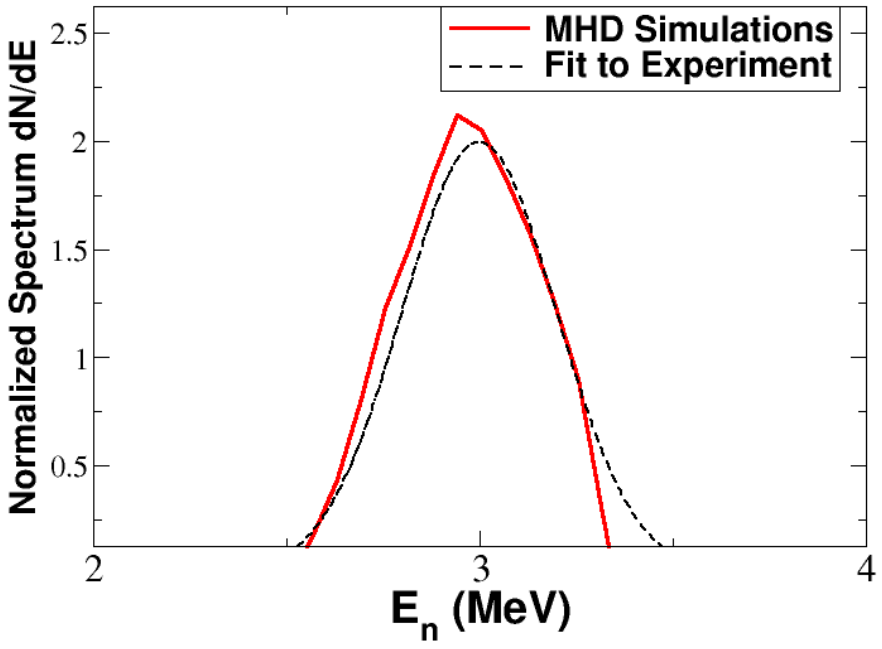

Figure 4: The predicted neutron energy distribution for DD neutrons for a DPF setup in which the INNY was placed 5 cm from the anode. The dashed curve is a Gaussian fit to the experimentally determined energy distribution.

tend to break-up the sheath front surface and, thus, influence the position at which the pinch is formed.

In Fig. 4, we show the predicted energy distribution for DD neutrons for the case where the INNY is included and positioned 5 cm from the anode. On average, we see an upshift of the DD neutrons to 2.95 MeV, with an energy width that is very approximately described by by a Gaussian width $\sigma = .2$. However, we predict very few neutrons above 3.5 MeV, and our distribution is not symmetric. A very small number of neutrons are produced form secondary DT reactions, in which the 1 MeV tritons born in the DD reaction undergo DT reactions. However, this component of the spectrum is less than 10^{-4} of the total and it relative magnitude is not predicted accurately by the current simulations. Also, shown in Fig. 4 is a Gaussian fit to the experimental energy distribution, which was obtained [9] by fitting the neutron activation observed in a set of energy-thresholding targets placed inside the INNY, at about 6.5 cm from the anode. The experimental measurements also saw some evidence for a very small 14 MeV neutron peak, most likely from secondary DT reactions. The close agreement between theory and experiment for the main neutron production lends strong support to the fidelity of the MHD calculations and our neutron post-processing simulation method/tool. We also examined the effect of K-H instabilities on the neutron production, by reducing the resolution of the simulations to the point that K-H instabilities

were no longer predicted. Comparisons between the low and high resolution calculations suggest that the K-H instabilities affect the magnitude and time and energy shape of the neutron pulses at about the 20% level.

6 Effects of Variations in the INNY design

6.1 Pinch formation without the INNY: Long, multiple neutron pulses

When no INNY is included in the DPF setup, we find that the current sheath gradually collides at the $r = 0$ axis, but that multiple pinches form. The first pinch forms closet to the anode, and the later additional pinches form progressively further from the anode surface. This is shown in Fig. 5, where we show a simulation with the INNY placed at 10 cm from anode, which is sufficiently far that the sheath evolution is unaware of the existence of the INNY. In this configuration, three successive pinches are formed, between $t = 0.472 - 0.568$ μs, with three corresponding peaks in the neutron time history.

Our main conclusion from our MHD simulations without the inclusion of an INNY is that the experimentally observed multiple and long-lasting neutron pulses originate form the formation of multiple, time-separated pinches. This interpretation strongly suggests that we can control the neutron pulse by limiting the number of pinch formations that can occur, through an optimally positioned and sized INNY. In the next sections we investigate different INNY to anode distances and INNY diameters.

6.2 Effects of different INNY to anode distances

To explore the pinch formation dynamics in the presence of an INNY, we simulate several different INNY to anode distances. When the INNY is very close to the anode, relatively little current sheath material and magnetic field strength can propagate into the region between the two, and the resulting pinch is weak. On the other hand, when the INNY is located too far from the anode, multiple pinches can form. This suggests the existence of an optimal INNY to anode distance, at which the pinch formation is still relatively strong but its time duration is limited. Fig. 6 shows the predicted neutron production history for different INNY heights.

To quantify the situation, we use one INNY radius ($R_{Inny} = 7.6$ cm) and vary its height above the anode. We find that there is an optimum INNY to anode distance, namely at 6.5 cm. There, we find that a single main pinch is formed, with both strong density and magnetic fields. These conditions are ideal for producing neutrons, as shown in Fig. 7. We note that this INNY position is 1.5 cm further from the anode than the experimental position that has been used to date. However, from our detailed analyses we suggest that this increased INNY-to-anode distance be incorporated in all new DPF designs.

As seen in Fig. 6, some INNY distances result in a main pulse plus a smaller pulse, such as that seen for $H_{Inny} = 5$ cm in Fig. 8. The smaller pulse can be either before (a 'front porch') or after (a 'back porch') the main pulse, depending on the INNY-to-anode distance. As the INNY moves further away from the anode, the timing of the formation of the first

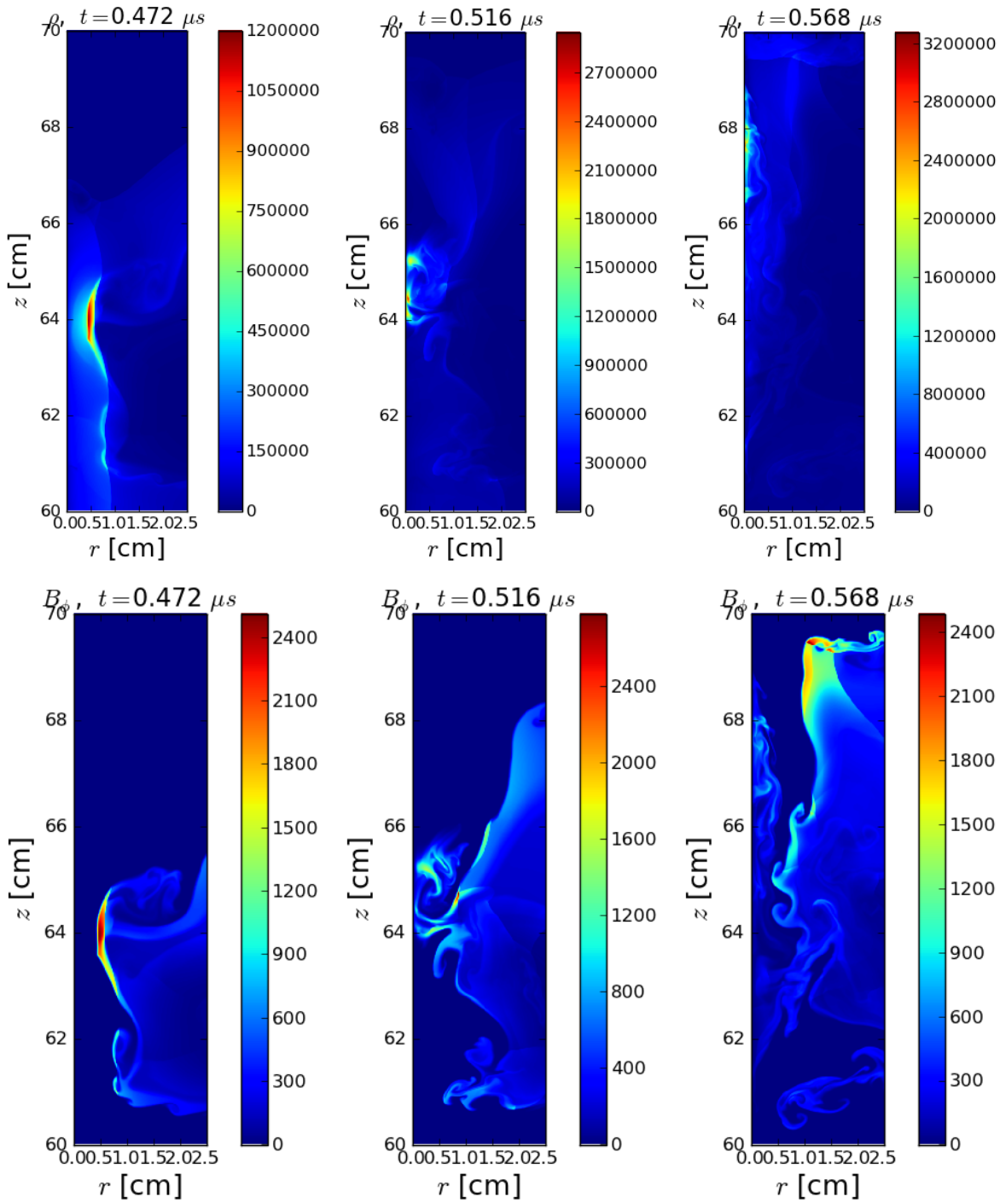

Figure 5: The density plots (top row) and magnetic field (bottom row) for an INNY to anode distance of $H_{Inny} = 10$cm. The corresponding neutron time history involves three peaks at $t = 0.472\mu s$, $0.516\mu s$, and $0.568\mu s$. The predicted peaks coincide well with the formation of successive pinches.

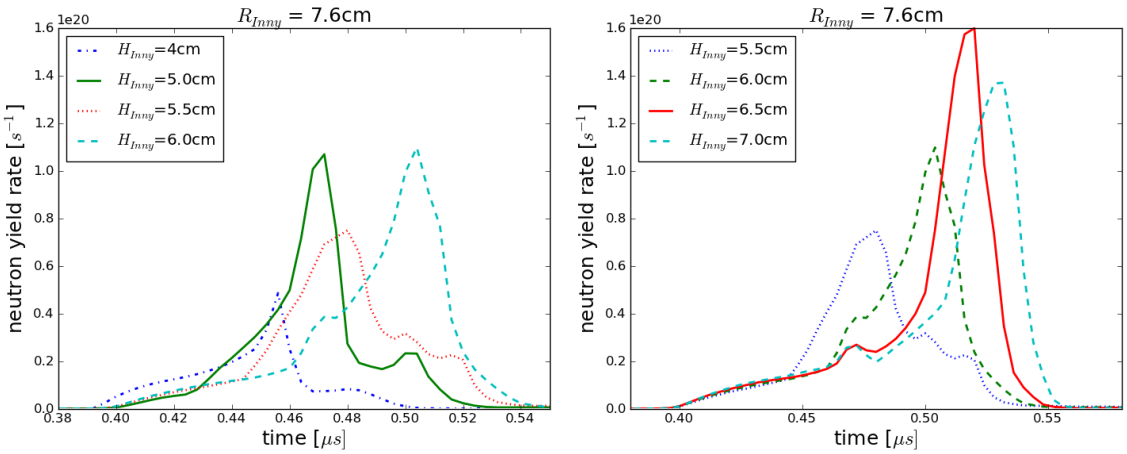

Figure 6: Neutron production history for different INNY heights. These represent a scan of INNY distances with their corresponding neutron time histories. The most ideal and dominant peak in neutron time history occurs at an INNY distance of 6.5 cm and corresponds to the formation of one main pinch only.

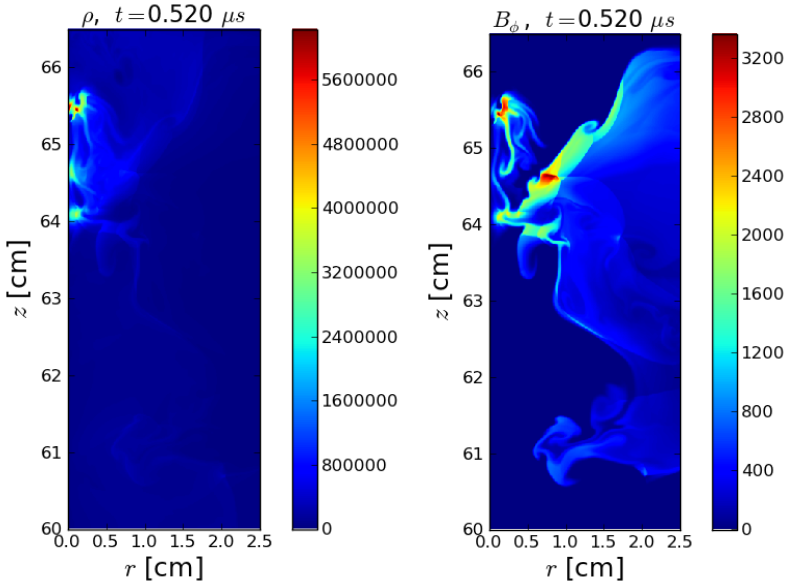

Figure 7: The density and magnetic fields for $H_{Inny} = 6.5$ cm. The neutron production rate has a peak value at $t = 0.52\mu s$.

pinch is not affected by the presence of INNY. This is seen in Fig. 6 for $H_{Inny} = 6.5$ and 7 cm. The first neutron peak always appears at $t = 0.472\mu s$, but the second peak moves to a later time as the INNY moves further out. This time shift happens because, as the INNY moves out, the second pinch moves higher up the z axis and also lasts longer. We were unable to find an INNY position that totally eliminated either a front or back porch. Thus, we

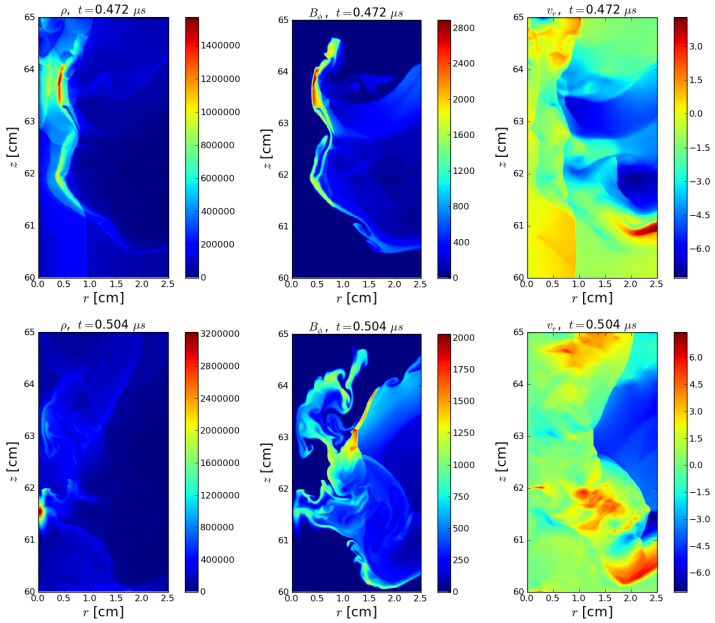

Figure 8: The density (left), magnetic field (middle) and radial velocity (right) for $H_{Inny} =$ 5.0 cm at two different times, $t = 0.472\mu s$ (top row) and $t = 0.504\mu s$ (bottom row). These two times correspond to the main neutron production, where the main peak and a smaller later peak are produced. Strong neutron production typically requires that the product of density, magnetic field and radial velocity is large.

recommend that any analysis of neutron activation of objects using the DPF accommodate these porches.

6.3 Effects of different INNY sizes

We next examine whether there is an optimum INNY size (radius) that should be considered for new tube designs. Fig. 10 shows how the pulse shapes vary with the radius of the INNY, when the INNY is placed at 5 cm from the anode surface. We find that the pinch gets weaker as the INNY gets smaller, because a smaller amount of energy is trapped between the anode and INNY. Fig. 12 shows that the location of the main pinch is indeed similar for all four INNY sizes. Thus, the timing of pinches will remain the same for different sized INNYs, but the strength of the neutron pulse will be reduced with smaller INNYs. Thus, we recommend that the INNY be designed to be the maximum possible width across the cathode opening, thus closing the 'outlet' in Fig.1.

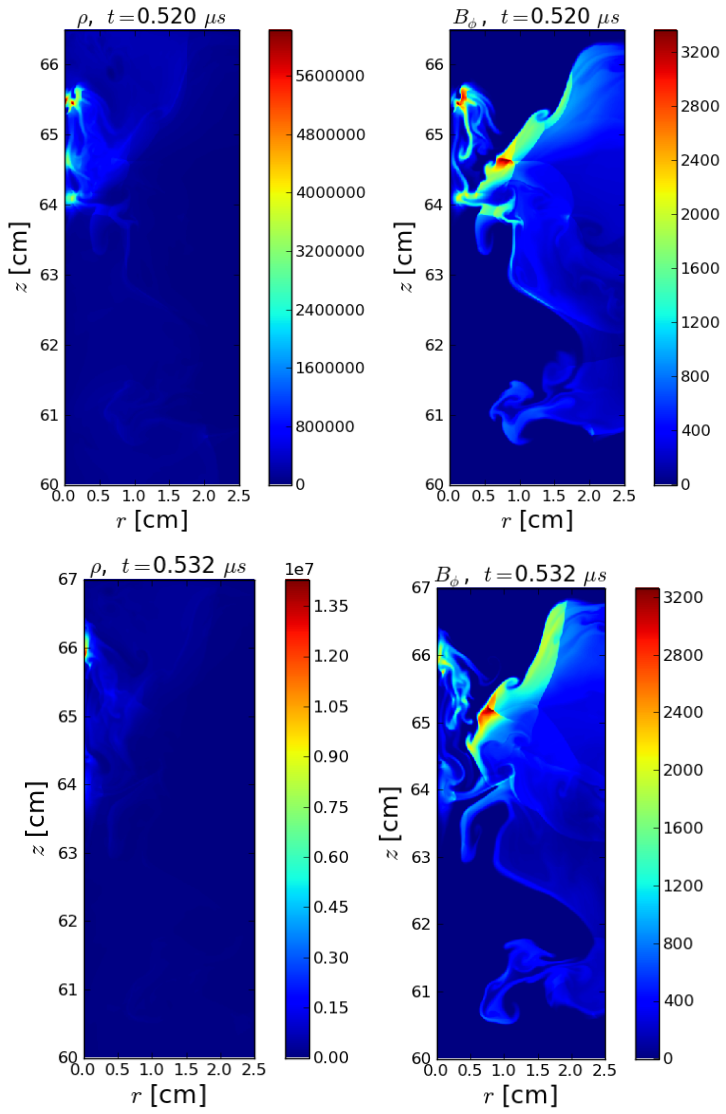

Figure 9: The density (left) and magnetic field (right) for $H_{INNY} = 6.5$ cm (top) and 7 cm (bottom) at $t = 0.504\mu s$. For the larger values of H_{INNY}, the main pinch moves higher up the z axis, further from the anode.

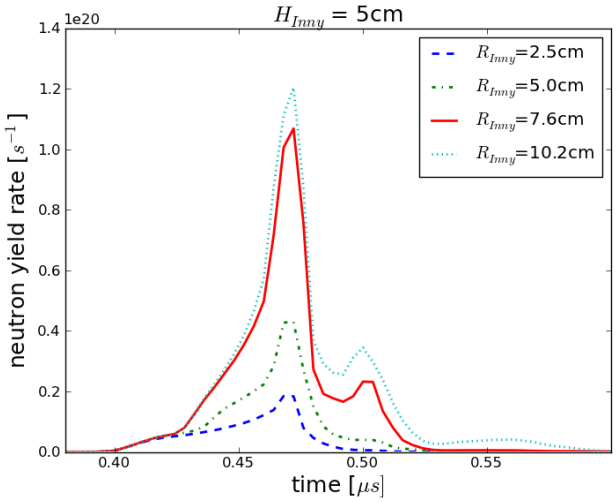

Figure 10: Neutron production history for different INNY widths R_{Inny}. The largest INNY produces the most neutrons since, in that case, all of the injected energy gets trapped in this case. However, we note that the timing of the neutron main peaks are essentially the same for all cases, suggesting that the pinch formation time is primarily determined by the INNY-to-anode distance, and not by the INNY size.

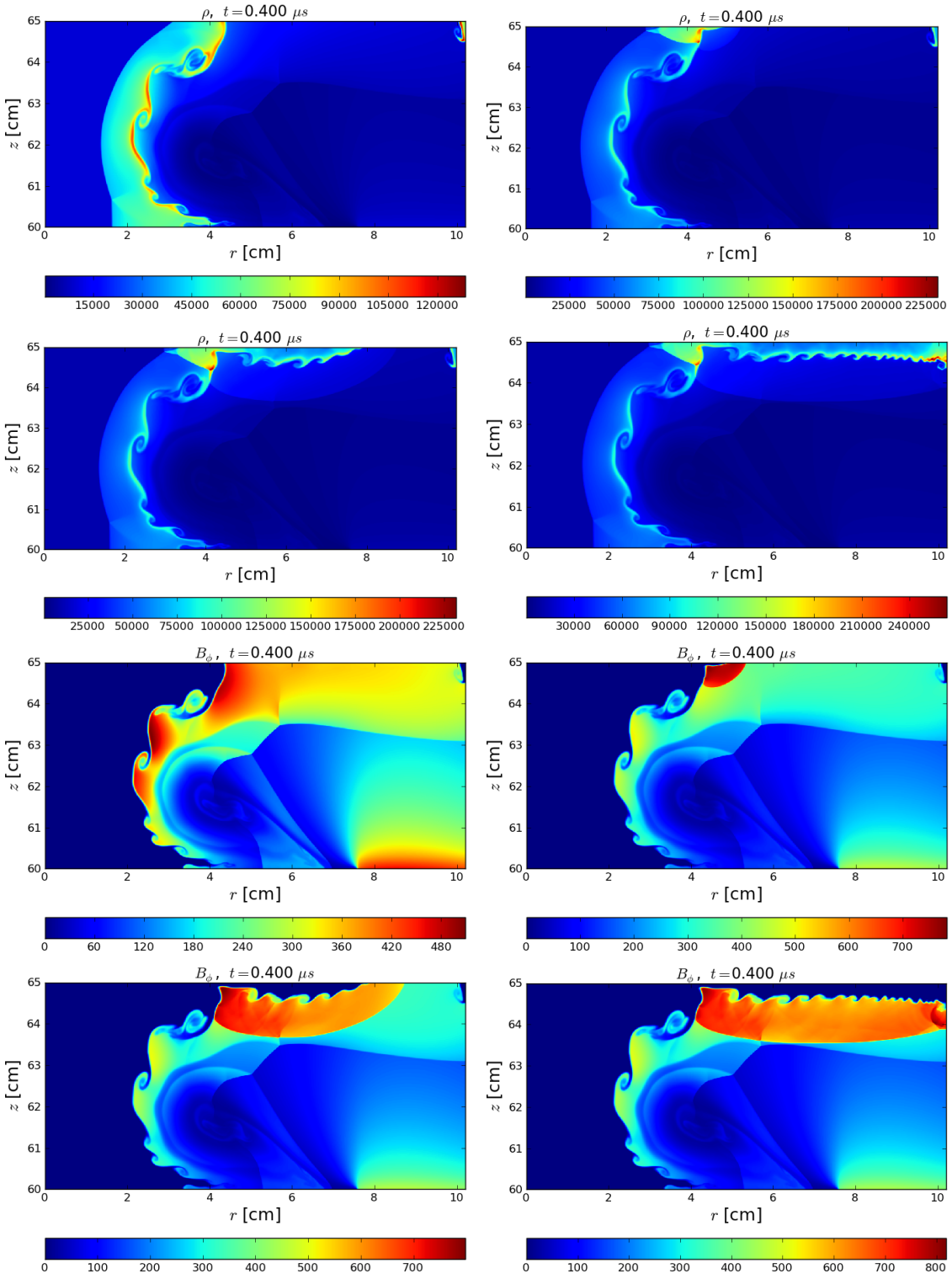

Figure 11: Comparison of the density (ρ, upper four figures) and magnetic field components (B_ϕ, lower four figures) for different Inny sizes. R_{Inny}: 2.5 cm, 5.0 cm, 7.6 cm, and 10.2 cm.

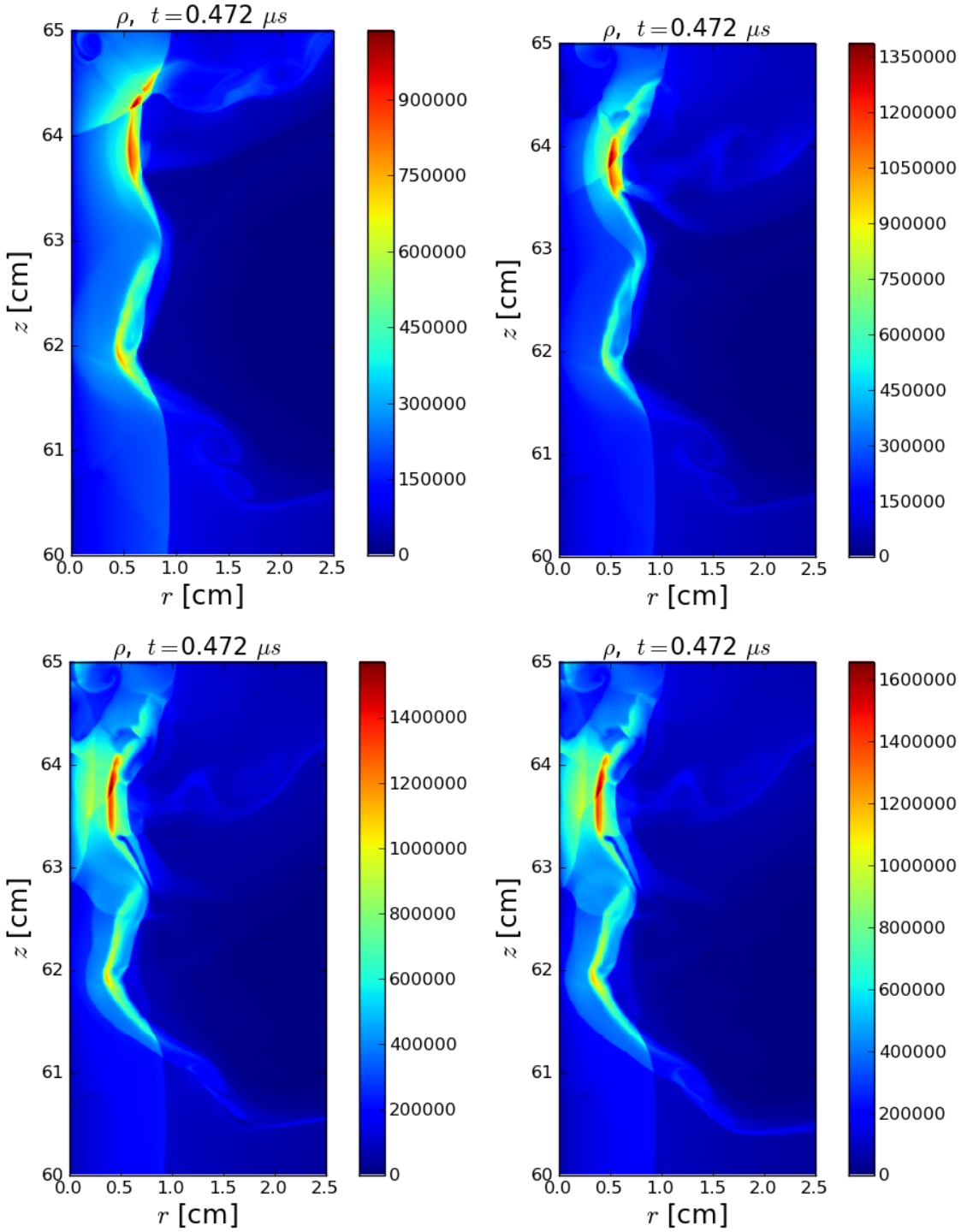

Figure 12: Density at neutron peak production, for different Inny sizes. R_{Inny}: 2.5 cm, 5.0 cm, 7.6 cm, and 10.2 cm.

7 3D MHD Results

Experimental results have shown clear azimuthal asymmetries for the current sheath front, as shown in Fig. 13. In fact, the front speeds are observed to be different at different azimuthal angles. This affects the location of the pinch with respect to the axis of the anode.

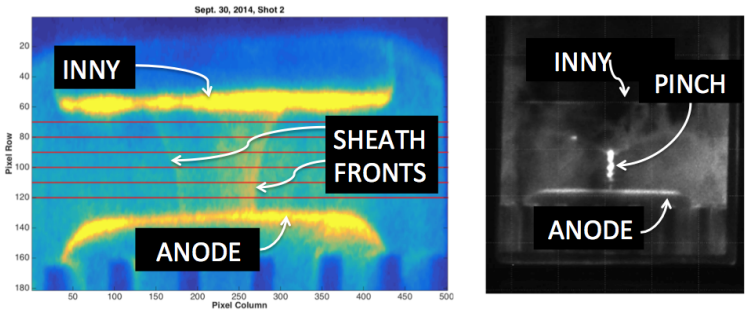

Figure 13: Optical images showing the azimuthal asymmetries during the run-in phase (left) and screw-like pinch during the pinch formation phase. Figures courtesy of Nevada experimental team [10].

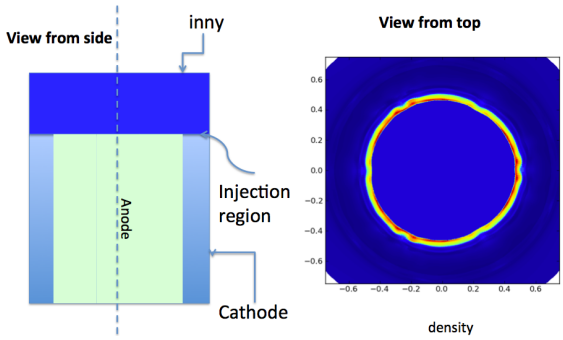

Figure 14: 3D MHD simulation set-up. At the beginning of the simulation, a small perturbation (5%) was added to the density in the current sheath front, as seen on the right panel. The spatial normalization is such that 1 unit corresponds to 10 cm.

We carried out 3D MHD LA-COMPASS simulations of DPF dynamics using the set-up shown in Fig. 14, examining asymmetries by introducing 3D perturbations on the sheath fronts. We find that small amplitude perturbations at large radius $r \sim 5$ cm lead to a very different final density and magnetic field distributions, as shown in Fig. 15. The amplitude of the pinch, its radial location, and its vertical location all show marked differences between the 2D and 3D simulations. More importantly, the instability associated with the pinch is now a kink instability, unlike the 2D simulations where only sausage mode instabilities are allowed. The situation is depicted in Fig. 16, where the current intensity is shown to be very non-cylindrical. The pinch is poorly formed and is also produced far off the $r = 0$ central axis. The corresponding neutron production is also weak. These effects have been

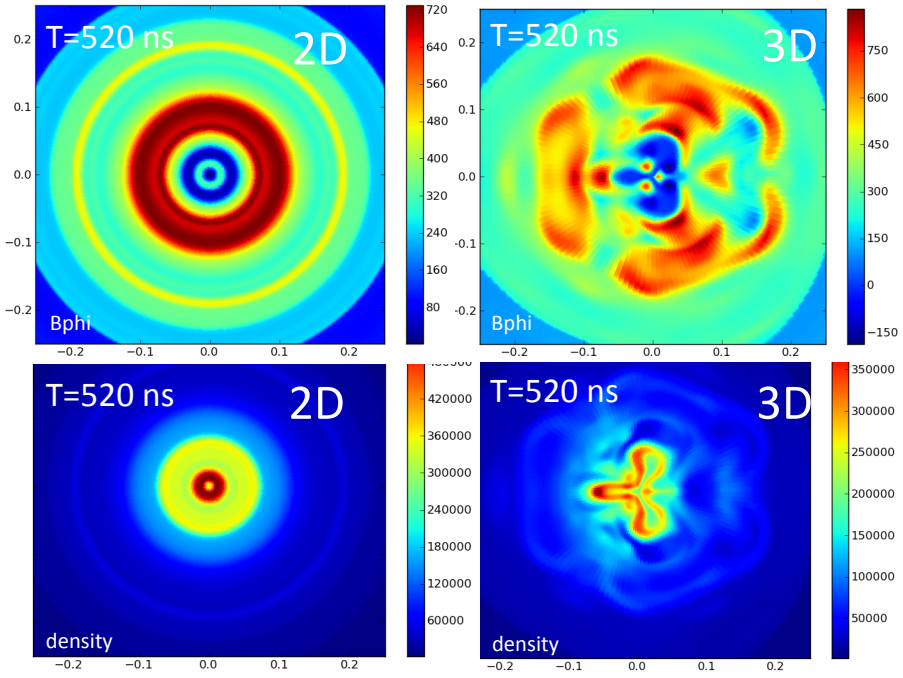

Figure 15: Comparison between 2D and 3D simulations with the same injection parameters and set-up, except that a 5% perturbation is added in the 3D simulation around $r \sim 5$ cm. The top row is for the magnetic field component B_ϕ and the bottom row is for the density. The spatial normalization is such that 1 unit corresponds to 10 cm.

seen experimentally, where 3D asymmetries have led to poor pinches or no pinches, and a large divot is observed in the top of anode, more than a centimeter from $r = 0$.

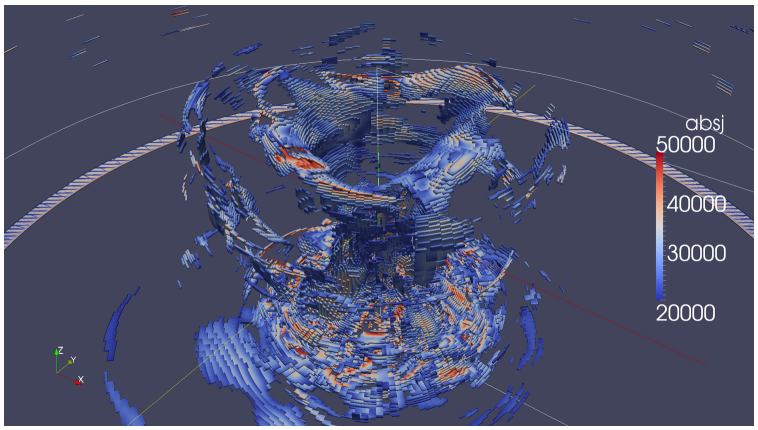

Figure 16: The total current intensity at the pinch based on 3D MHD simulation, showing the 3D nature of the pinch and development of kink instability.

The cause of the asymmetries is unclear and requires further experiments. One possibility is that unwanted fluorescent effects from impurities is ionizing gas in front of the sheath, and thus causing the sheath velocity to be different at different azimuthal angles. What our simulations can say is that perturbations at the 5% level in the sheath velocity fronts will lead to 3D kink instabilities. Sparks induced by the existence of impurities can further disrupt the system and the resulting mechanical forces can cause the anode and cathode to be no longer concentric. Once this happens, the DPF device is unlikely to produce useful neutron pulses and the tube will have to be replaced. Thus, we strongly recommend that impurities be avoided. This includes insuring that sealants not contain compounds that are likely to fluoresce.

8 Summary

We have carried out a series of 2D and 3D high-fidelity MHD simulations for the pinch formation in DPF devices. In these simulations, we varied a number of design parameters, including the size and position of the INNY. We simulate the neutron production via a post-processor and find very good agreement between theory and experiment for the time shape of the neutron pulses and their energy distribution. We make a number of recommendations for future DPF tube designs, which are:

- Comparisons between predicted and measured neutron energy and timing distribution for current DPF setups should be used to assess the accuracy of models.
- The INNY should be placed at 6.5 cm from the top of the anode.
- The INNY diameter should be large enough to cut off any exit of energy or ions from the region between the anode and the INNY.
- 3D asymmetries can cause device failure and must be analyzed. In particular, 3D sheath velocity asymmetries should be minimize.
- Impurities that can induce fluorescence or sparking should be avoided, as these exaggerate asymmetries in sheath propagation.

References

[1] N. Bennett, National Security Technologies DPF Team, private communication.

[2] Li, S. and Li, H. *A Modern Code for Solving Magneto-hydrodynamic or Hydrodynamic Equations*, Technical Report, LA-UR-03-8928 (2003)

[3] Li, S. and Li, H. *A Fast Parallel Simulation Code for Interaction between ProtoPlanetary Disk and Embedded Proto-Planets*, Technical Report, LA-UR-09-2968 (2009)

[4] Li, S. and Li, H. *A Fast Parallel Simulation Code for Interaction between Proto-Planetary Disk and Embedded Proto-Planets: Implementation for 3D Code*, Technical Report, LA-UR-12-22213 (2012)

[5] Li, H. et al., *Modeling the Large-Scale Structures of Astrophysical Jets in the Magnetically Dominated Limit*, Astrophysical Journal, 643, 92 (2006)

[6] Nakamura, M., Li, H., & Li, S. "Structure of Magnetic Tower Jets in Stratified Atmospheres", Astrophysical Journal, 652, 1059 (2006)

[7] Nakamura, M., Li, H., & Li, S. "Stability Properties of Magnetic Tower Jets", Astrophysical Journal, 656, 721 (2007)

[8] Jungman, G. and Hayes, A.C. *The Relationship between Charged-Particle Fluence and Stopping Power*, Los Alamos Internal Report, LA-UR-13-26171 (2013)

[9] R.S. Rundberg, private communication.

[10] These figures were provide by Chris Hagen and National Security Technologies DPF Team.